YTUP

Journal of Thermal Engineering
https://jten.yildiz.edu.tr/
https://doi.org/10.47481/jten.0062

RESEARCH ARTICLE

Analysis of isentropic efficiencies of ejector components in dual-evaporator refrigeration systems using CFD and experiments

Mahmut Cüneyt Kahraman[1,*], Ümit İşkan[2], Mehmet Direk[3]

[1]Yalova University, Department of Energy Systems Engineering, 77200 Yalova, Türkiye
[2]Yalova University, Yalova Community College, Electric and Energy Department, 77200, Yalova, Türkiye
[3]Yalova University, Department of Energy Systems Engineering, 77200 Yalova, Türkiye

Abstract

This study investigates the isentropic efficiencies of the main ejector components in a constant-pressure ejector used in a dual-evaporator refrigeration system. Experimental measurements were obtained from the test facility and computational fluid dynamics was used to support the numerical analysis. Main aim of this study was to the develop of empirical correlations for estimating ejector outlet enthalpy and part isentropic efficiencies at different condenser temperatures. In addition, the influence of mixing chamber and diffuser efficiencies on the performance of the second evaporator was examined. Isentropic efficiencies were decided for the motive nozzle, secondary flow outlet, suction chamber, mixing chamber, and diffuser for the selected ejector geometry. The results prove that increasing condenser temperature led to lower efficiencies in the motive nozzle and secondary flow outlet, however the suction chamber, mixing chamber, and diffuser showed improved performance. A similar trend was seen in the second evaporator. Higher condenser temperature and diffuser efficiency reduced the degree of superheat, while the cooling effect remained nearly unchanged over part of the operating range. The calculated isentropic efficiencies ranged between 0.80 and 0.95 for the motive nozzle, suction chamber, mixing chamber, and diffuser. By contrast, the secondary flow outlet showed a much wider variation, decreasing from 0.99 to 0.60. As condenser temperature increased, the degree of superheat dropped significantly, from 8.74 K to 0.19 K, while the cooling capacity of the second evaporator decreased from 68.02 to 55.07 kJ kg^{-1}.

Keywords: Ejector, CFD, isentropic efficiency, condenser, refrigeration

Cite this article as: Kahraman, M. C., İşkan, Ü., & Direk, M. (2026). Analysis of isentropic efficiencies of ejector components in dual-evaporator refrigeration systems using CFD and experiments. Journal of Thermal Engineering, 12(5), 1734–1747. https://doi.org/10.47481/jten.0062

1. Introduction

Ejector energy losses play a critical role in deciding the overall performance of ejector-based refrigeration systems. Earlier studies have shown that system performance can be improved by finding the isentropic efficiencies of individual ejector components and then addressing the main sources of loss [1, 2]. Among the parameters commonly used to evaluate ejector performance, the entrainment ratio (ER), pressure ratio, and component-level efficiencies are the most widely reported [3, 4]. Fan et al. [5] examined how compressor frequency and the pulse number of the electronic expansion valve (EXV) affect the performance of a dual-evaporator refrigeration system. Their results showed that changes in EXV pulse number had little influence on either cooling capacity or coefficient of performance (COP). Other studies have focused more directly on ejector design and its effect on system behavior. For example, Li et al. [6] investigated a refrigeration system running with R1234yf and R134a using a constant-pressure ejector. They reported that several design-related parameters, including the suction nozzle pressure drop, area ratio, and ejector part efficiencies, had a strong influence on system performance. Furthermore, researchers have focused on the isentropic efficiencies of several ejector components. Liu and Groll [7] reviewed these studies and reported that the calculated efficiencies ranged from 0.7 to 0.95. Table 1 summarizes the results of these studies.

In addition to overall system indicators, extra attention has been given to the isentropic efficiencies of specific ejector

*Corresponding Author
E-mail Adress: mcuneyt.kahraman@yalova.edu.tr

Submitted: 17 February 2025; **Accepted:** 10 July 2025

This paper was recommended for publication in revised form by Editor-in-Chief Ahmet Selim Dalkılıç

sections. Since the internal flow structure of an ejector is highly sensitive to geometry, direct experimental measurement of local flow parameters is difficult. For this reason, experimental work is often supported by numerical analysis. CFD has become a widely accepted tool for examining complex ejector flow behavior and for estimating the efficiencies of individual components [2, 5]. Using a combined experimental and numerical approach, Banasiak et al. [8] investigated the optimum ejector geometry for an R744 heat pump system. Their study showed that replacing the conventional expansion valve with an ejector improved the COP by approximately 8%. Focusing on modelling, Ünal et al. [9] developed a mathematical model to assess the performance of a refrigeration cycle with an ejector. Their model investigated the influence of the inlet velocities of the mixing section (for suction flow) and the diffuser outlet velocities on the system performance They reported that incorporating these velocity effects resulted in a 5.8%-7% increase in cooling capacity compared to a model neglecting velocity effect. A study by Galanis and Sorin [10], found the critical pressure ratio and mixing chamber efficiency by developing a one-dimensional thermodynamic model of the ejector using the results of experimental and CFD analysis. Their work additionally revealed that mixing, normal shock waves, and subsonic frictional flows within the ejector contribute to entropy generation. Further insight into the relationship between ejector geometry and system performance was provided by Liu et al. [11], who used a two-dimensional axisymmetric model to examine how the area ratio affects both overall ejector behavior and the efficiencies of individual components. Their results showed that, among the internal sections of the ejector, the mixing chamber was particularly sensitive to changes in area ratio and played a more influential role in overall performance than the other components. Another study on the two-phase ejector efficiencies of several parts was performed by Wang and Yu [12]. The researchers reported that the efficiencies of the motive nozzle, mixing chamber, and diffuser under the specified conditions were in the range of 0.513-0.750, 0.492 0.755, and 0.610-0.734, respectively. Moreover, this study suggested empirical correlations for efficiency calculations of several parts of the ejector. Zhang et al. [13] used CFD analysis to examine how surface roughness influences the efficiencies of different ejector components. By separating the ejector into five distinct regions, they set up a correlation between surface roughness and part efficiency and proposed a corresponding correlation coefficient for each section. Kitrattana et al. [14] employed a vapor ejector model based on Stoecker theory for design and performance analysis. They compared the results obtained from this model with those from the classical one-dimensional ejector model (Keenan's model) which is based on ideal gas. The comparison focused on critical condenser pressure, ER, and geometry. The authors reported good agreement between the two models when compared to experimental data. Bauzvand et al. [15] further examined how operating conditions affect ejector performance. Their study focused on the influence of ejector back-pressure ratio and the volumetric flow rate of the primary stream on overall ejector efficiency. The results showed that both parameters were positively correlated with ejector efficiency. In a similar way, other researchers [7] have developed predictive correlations for estimating the efficiencies of individual ejector components based on ejector geometry and flow conditions. Zhang et al. [16] investigated the performance of several turbulence models to predict the isentropic efficiencies of several ejector components. Their investigation showed that the SST k-omega turbulence model provided the most reliable predictions across a wide range of ejector geometries and operating conditions. In a similar study, Bumrungthaichaichan et al. [17] applied the SST k-omega model to simulate velocity distribution and turbulence behavior inside the ejector, reporting good agreement between the numerical predictions and experimental measurements. Three-dimensional ejector models have also been widely used and confirmed against experimental data. These studies consistently show that the SST k-omega model performs better than alternative turbulence models in capturing both overall flow behavior and local flow structures within ejectors under different geometrical configurations and operating conditions [18]. Rand et al. [19] used numerical simulations and conducted experimental studies to analyze the effect of outlet position of nozzle head on ejector performance. RANS model successfully predicted the complex relationship between ER and nozzle head outlet position. Atmaca and Ezgi [20] further proved the usefulness of CFD for ejector analysis by developing a three-dimensional model of a steam ejector to examine static pressure and velocity distributions. Their numerical results showed good agreement with analytical data, reinforcing the value of CFD as a practical tool for ejector studies, particularly because it allows extensive parametric analysis within a relatively short time once the model has been confirmed.

Earlier studies have examined the isentropic efficiencies of ejector components, with attention given to the effects of geometry and operating conditions. However, the effect of condenser temperature on these efficiencies, and its influence on system performance, has received comparatively limited attention. To address this gap, the present study combines experimental measurements with CFD analysis to evaluate the efficiencies of individual ejector components under different condenser temperatures. In addition, new empirical correlations are proposed to predict ejector efficiencies while explicitly accounting for the effect of condenser temperature. Finally, the impact of varying ejector efficiency on system performance parameters is analyzed. This work distinguishes itself by proposing an empirical method to derive equations for deciding the isentropic efficiency of ejectors with diverse geometries. For all these analyses, seven steps are followed, which are detailed in Section 2.1 Methodology.

Table 1. Isentropic efficiency values of the several parts of the ejector obtained from the several research

Authors	Fluid	η_{mn}	$\eta_{suction}$	η_{mc}	η_d
Liu and Groll [7]	CO_2	0.5-0.93	0.37-0.9	0.5-1	-
Vereda et al. [21]	Ammonia/ lithium nitrate	0.85	0.85	0.9	0.8

Ameur et al. [22]	R134a	0.86	0.86	0.78	0.8
Ameur and Aidoun [23]	CO_2	0.86	0.86	0.78	0.8
Kitrattana et al. [14]	Steam	0.9	-	0.9	0.9
Zheng et al. [24]	CO_2	0.8	0.8	0.8	0.8
Wang et al. [25]	R1234yf	0.85	0.95	0.85	-
Surendran and Seshadri [26]	R1234yf	0.7	0.7	0.7	0.7
Bilir and Ersoy [27]	R134a	0.9	0.9	0.9	0.8
Ünal and Yilmaz [28]	R134a	0.9	-	0.8	0.9
Chen et al. [1]	R123, R141	0.9	-	0.85	0.9

2. Material and method

The experiments were carried out using a DEES consisting of two evaporators (one water-cooled and one air-cooled), a compressor, an air-cooled condenser, a constant-pressure ejector, a thermostatic expansion valve (TXV), thermocouples, flowmeters, anemometers, and pressure gauges. Notably, both the ejector and the second evaporator (evaporator #2) are unique components of a DEES system, not typically found in a conventional vapor compression refrigeration cycle. A hermetic Danfoss compressor (30.23 $cm^3 \cdot rev^{-1}$, 2900 rpm) was selected as a compressor for the experimental setup. Figure 1 illustrates the equipment layout and the refrigerant flow paths within the DEES system. The employed constant pressure ejector, designed to enhance system performance by raising the compressor inlet pressure of the refrigerant, is depicted with its dimensions in Figure 2 [29,30]. The ejector geometry was decided through a literature review of systems with comparable cooling capacities [31, 32]. During the experiments, the refrigerant flow rates entering the first and second ejector inlets were regulated using valves B and C (Figure 1). Valve B was kept fully open throughout the tests to keep stable pressure at the primary inlet. The desired flow split was achieved by partially opening valve C. As the refrigerant after entering the TXV, a slight pressure drop at this stage is not critical. The equal distribution of flow was measured using a turbine flowmeter positioned upstream of the first ejector inlet. Due to the inherent sensitivity of the flowmeter and the manual adjustment of the valves, the actual flow split ratio is reported as a range.

Figure 3 presents diagram of the experimental setup. The air-cooled condenser was placed in an air duct, and an adjustable centrifugal fan was used to precisely control condenser air flow rates. An electric heater was used to regulate the condenser air temperature. PID controllers kept the desired condenser air conditioning. This arrangement made it possible to control the compressor outlet pressure by adjusting the target condensation temperature. Evaporator #1, the air-cooled unit, was placed in a separate duct with characteristics like those of the condenser section. Evaporator #2 was designed as a water-source heat exchanger and is also shown in Figure 3 together with its dedicated water loop and storage tank. Both the water flow rate and inlet temperature in this loop were carefully controlled. Water and refrigerant mass flow rates were measured using high-accuracy instruments: an electromagnetic flowmeter (±0.3%) for water and a Coriolis flowmeter (±0.05%) for refrigerant.

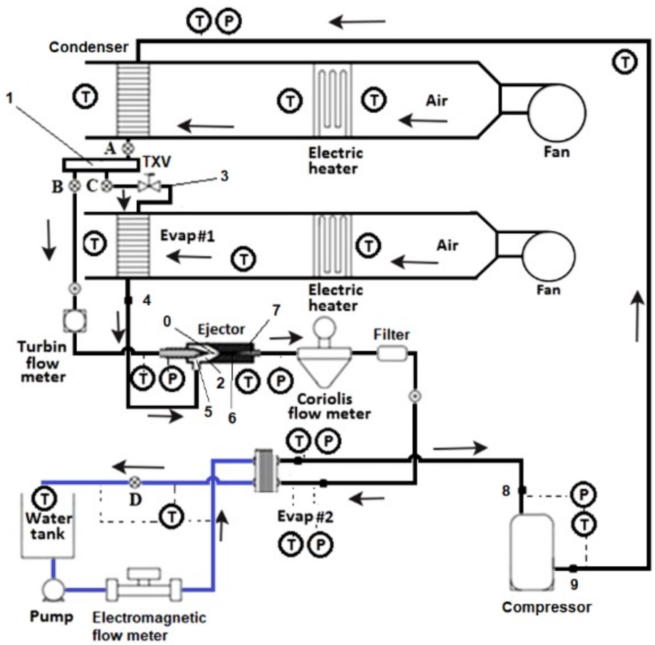

Figure 1. DEES equipment and the refrigerant paths [33]

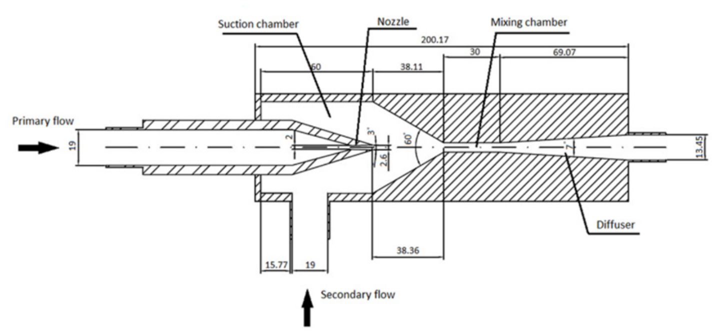

Figure 2. Dimensions of the ejector [33]

In addition, a turbine flowmeter (±0.1% accuracy) was used at the primary inlet of the ejector to measure the refrigerant mass flow rate. Temperatures of refrigerant and water were checked at the inlet and outlet of each part. K-type thermocouples connected to a 40-channel data acquisition system are used for temperature measurements. Refrigerant pressures at different locations in the test rig were recorded using digital manometers (±0.5% accuracy) and pressure transmitters. A detailed assessment of sensor accuracy and sensitivity is provided in Reference [29]. Based on that analysis, the overall experimental uncertainty of the DEES was determined to be below 1.00% [29].

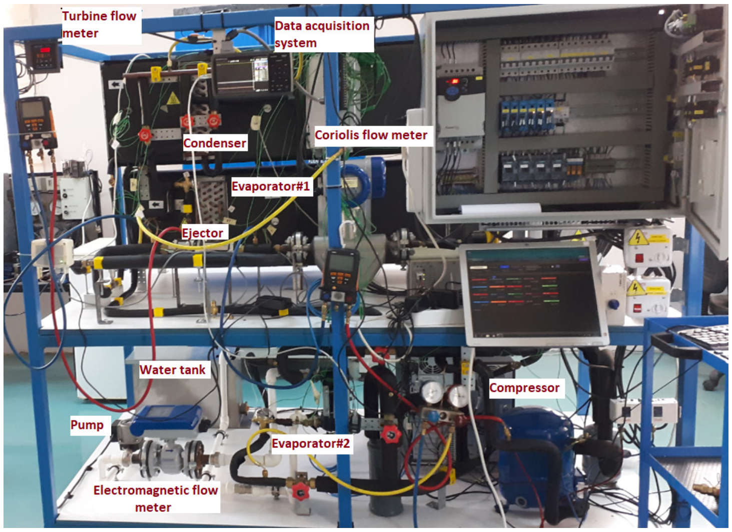

Figure 3. Test setup and the test components [29]

2.1. Methodology

The authors followed the steps given below in this study, respectively.

1. Experimental Study: The experimental investigation involved running the DEES setup under various condenser temperatures. Eleven different condenser temperatures, ranging from 25°C to 43°C, were investigated. To ensure consistent operating conditions, the air velocity across evaporator #1 was kept at 1 $m.s^{-1}$, while the ER was kept within the range of 0.50–0.55. Each test was repeated three times to confirm the reproducibility of the measurements.
2. CFD Model Validation: A mathematical model of the ejector was developed and solved using ANSYS Fluent code. To confirm the accuracy of the commercial CFD code, simulations were conducted to calculate the ejector outlet and inlet pressures and compared to experimental values.
3. Determination of Thermophysical Properties of Refrigerant within the Ejector**:** The pressure and quality values of the refrigerant throughout the ejector were decided by analyzing data extracted from the CFD simulations.
4. Determination of Thermophysical Properties of Refrigerant within the Ejector by an assumption**:** The thermophysical values of the points determined in Step-3 were calculated with the assumption that each part of the ejector was isentropic.
5. Isentropic Efficiency Calculations: The isentropic efficiencies of each ejector part were after decided by taking the ratio of the values obtained in step 3 to those obtained in step 4. Furthermore, new correlations were developed to predict these efficiencies, with condenser temperature serving as the sole variable.
6. Correlation Verification: The isentropic efficiency values calculated in step 5 were used to calculate the refrigerant's thermophysical properties at the inlet of evaporator #2. The results were compared with the data from experimental results to verify the accuracy of the correlations.
7. System Performance Analysis**:** The final stage involved analyzing the influence of variations in the isentropic efficiencies of various ejector components on the overall system performance parameters.

The isentropic efficiencies of the components of an ejector of varying dimensions can be obtained by applying the procedures described in the first five steps. These steps and corresponding instructions are illustrated in Figure 4 below.

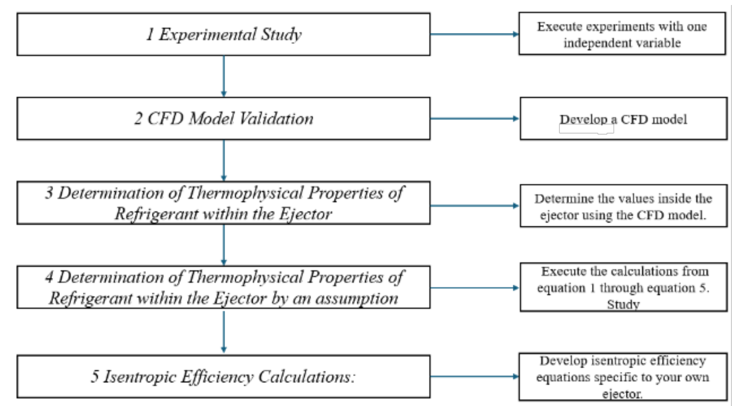

Figure 4. Procedures and instructions for isentropic efficiency calculations

2.2. Test procedure

The experiments were conducted at eleven condenser temperatures ranging from 25°C to 43°C. Condenser air temperature was adjusted using an electric heater installed inside the air duct. Data acquisition began once evaporator #2 reached a cooling capacity of 0.8 $kJ \cdot kg^{-1}$. To keep consistent operating conditions throughout the tests, the air velocity across evaporator #1 was fixed at 1 $m.s^{-1}$, while the ER was kept within the range of 0.50–0.55. The following assumptions were used during the experimental procedure:

- Isenthalpic operation of the TXV.
- Negligible pressure loss within evaporator#2.
- Adiabatic conditions between the ejector outlet and the compressor inlet.
- A thermal efficiency of 0.95 for the evaporator#2 plate heat exchanger.
- The refrigerant exiting the ejector matches the conditions at the evaporator #2 inlet.

2.3. Efficiency analysis of system and ejector

This section explains the method used to evaluate the efficiency of each ejector part. For the analysis, the ejector was divided into five sections: the motive nozzle, suction chamber, diffuser, secondary flow outlet, and mixing chamber as illustrated in Figure 5. Efficiency calculations were carried out using data from both experimental measurements and the CFD simulations. Following the determination of ejector efficiencies, system performance parameters such as cooling capacity and degree of superheat were analyzed. Figure 6, where key points are shown, presents a P-h diagram depicting the assumed isentropic operation of the system Point P_0 is the narrowest point of the ejector nozzle, where the pressure is the lowest. Due to the low pressure at this point, the refrigerant in the vapor phase (number 4) is drawn into the ejector and its pressure decreases. Since the ejector is a constant pressure ejector, the same pressure is expected from the ejector nozzle outlet to the mixing chamber outlet. In addition, the processes occurring inside the ejector are represented by red lines on the P–h diagram and those outside the ejector are shown in blue. The efficiencies of the individual ejector components were calculated by substituting the thermodynamic properties obtained from Figure 6 and the CFD results into Equations. 1-5 [2].

Motive nozzle isentropic efficiency is defined as:

$$\eta_{mn} = \frac{h_{0,is} - h_{2,sim}}{h_{2,is} - h_{2,sim}} \tag{1}$$

where is: isentropic, sim: simulation.

Secondary flow outlet isentropic efficiency is defined as:

$$\eta_{Sfo} = \frac{h_{5,is\text{-}a} - h_{5,sim}}{h_{4,is} - h_{2,is}} \tag{2}$$

$h_{5,is\text{-}a} = f(s_4, x=1)$

Suction chamber isentropic efficiency is defined as:

$$\eta_{sc} = \frac{h_{5,is} - h_{2,is}}{h_{5,sim} - h_{2,sim}} \tag{3}$$

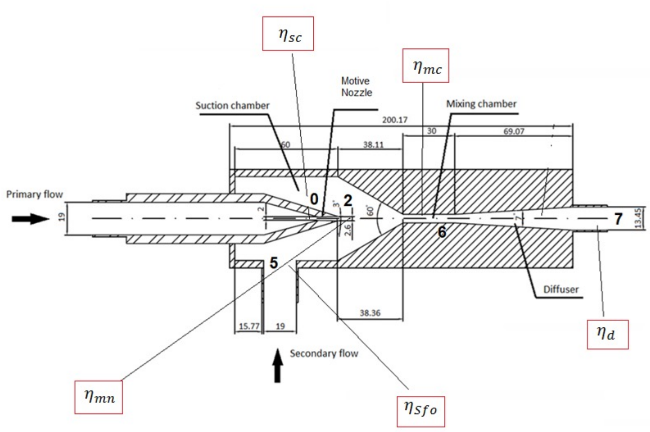

Figure 5. Various parts of the ejector

Mixing chamber isentropic efficiency is defined as:

$$\eta_{mc} = \frac{h_{6,is} - h_{2,is}}{h_{6,sim} - h_{2,sim}} \tag{4}$$

Diffuser isentropic efficiency is defined as:

$$\eta_{d} = \frac{h_{7,is} - h_{6,sim}}{h_{7,sim} - h_{6,sim}} \tag{5}$$

The cooling capacities [28] can be calculated from:

$$\dot{Q}_{evap\,1} = \dot{m}_3 \neg \sum (h_4 - h_3) \tag{6}$$

$$\dot{Q}_{evap2} = \dot{m}_{total} \cdot (h_8 - h_7) \tag{7}$$

Total mass flow rate ($\dot{m}_{total}$) can be found from:

$$\dot{m}_{total} = \dot{m}_3 + \dot{m}_2 \tag{8}$$

ER value [33] can be found as:

$$ER = \frac{\dot{m}_3}{\dot{m}_{total}} \tag{9}$$

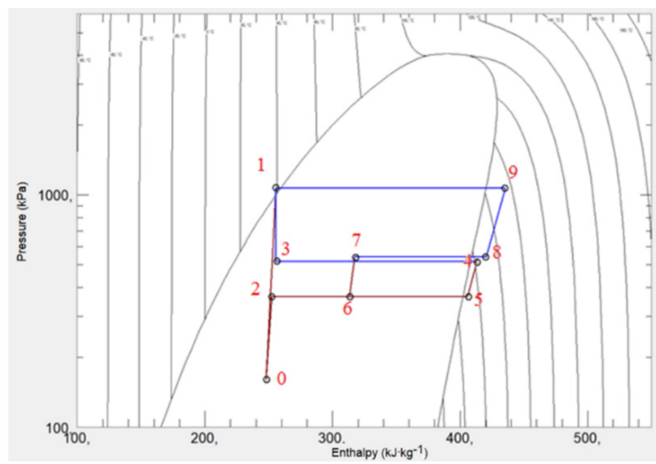

Figure 6. P-h diagram of the isentropic system

2.4. CFD model

This section details the physical and mathematical model of the CFD method used. While measurement devices were employed in the test setup, some areas within the ejector were inaccessible for physical measurements. Specific thermo-physical properties of the refrigerant were decided based on the CFD results. Additionally, the validation of the CFD code by comparison of experimental and CFD result is reported.

2.4.1. Physical model and grid convergence study

The geometry of the ejector, as depicted in Figure 2, was created using the CAD software SpaceClaim. The 2D geometry was then discretized into grid elements using ANSYS grid software. Prior research on ejectors suggests that a grid number between 80,000 and 90,000 elements is sufficient to achieve grid independence [34, 35]. In this study, additionally, three distinct grid sizes were analyzed to ensure grid independence. During mesh generation, the grid parameters were carefully controlled to provide high mesh quality. A maximum skewness below 0.7 and a minimum orthogonality above 0.6 were targeted. The nozzle outlet pressure was calculated for each mesh size, and the results are presented in Table 2. As can be seen, the mesh resolution had no significant effect on the predicted pressure values. At a 95% confidence level, the average deviation between the results was only 0.96%, showing that the results are independence from mesh size.

In addition, a separate grid convergence evaluation was carried out following the procedure recommended by the Glenn Research Center of NASA [36]. In Table 2, the Normalized Grid Spacing column shows the spacing values divided by the spacing of the finest grid.

The order of convergence is initially calculated using Equation 10:

$$p = \frac{\ln\left(\frac{P_3 - P_2}{P_2 - P_1}\right)}{\ln r} \tag{10}$$

where P is the nozzle outlet pressure for various grid sizes, while r refers to the refinement ratio, as calculated using Equation 11:

$$r = \frac{h_2}{h_1} \tag{11}$$

here, h values are the grid size. The order of convergence is calculated using Equations 10 and 11 as follows:

p=1.693.

Richardson extrapolation uses the two finest computational grids to estimate the pressure value at nozzle outlet as grid size approaches zero, as described in Eq. 12:

$$P_{h=0} = P_1 + \frac{P_1 - P_2}{2^p - 1} \tag{12}$$

$P_{h=0}$ is calculated as 402.956 kPa. The GCI for the fine grid solution is decided using Eq.13. A safety factor of FS=1.25 is applied because p is estimated to use three grids.

$$GCI_{12} = FS + \left|\frac{P_1 - P_2}{P_1}\right| \frac{100\%}{2^p - 1} \tag{13}$$

Applying Eq. 13 to grids 2 and 3 results in GCI_{12} and GCI_{23} values of 0.250% and 0.809%, respectively. The asymptotic convergence range is decided using Eq. 14.

$$\frac{GCI_{23}}{2^p GCI_{12}} \tag{14}$$

The asymptotic convergence ranges approximately one, showing that the solutions remain well within this range.

The nozzle outlet pressure for the system is 402.956 kPa, with an error of 0.25% or ±1.0 kPa. These studies prove that the results are independent of grid size. Based on the investigations given above and computational cost considerations, a total mesh number of 86,200 was selected for later simulations. Mesh number of 86200 reduced computational time by 60% versus finest grid while keeping <1% deviation in key outputs. A denser mesh was applied near the inlets of the ejector, the nozzle, and the wall boundaries, as illustrated in Figure 7.

Table 2. Nozzle outlet pressure changes in several grid numbers

Grid Size (mm)	Grid Numbers	Nozzle Outlet Pressure (kPa)	Normalized Grid Spacing
0.10	343731	402.4	1
0.20	86200	400.6	2
0.30	38423	394.8	3

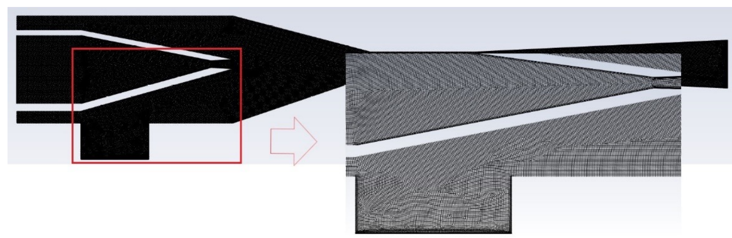

Figure 7. Grid structure of the ejector

2.4.2. Mathematical model

The commercial CFD software ANSYS Fluent (version 2019 R2) was used to develop the mathematical model of the ejector system and to solve the governing equations. A two-phase flow formulation was implemented to be the presence of a liquid phase at the primary inlet and a gas phase at the secondary inlet within the ejector. The Volume of Fluid (VOF) method was selected, as it has been shown to perform effectively in the steady-state simulation of two-fluid inlet configurations [37]. Turbulent effects were taken into consideration by using the k-ε realizable turbulence model with standard wall functions due to a well-established approach for resolving separation flows [38]. Prioritizing computational efficiency and validated accuracy, the k-ε realizable model with standard wall functions was found to yield sufficiently correct predictions for the overall flow behavior and performance parameters. The thermo-physical properties of the refrigerant (R134a) were obtained from the REFPROP software. The governing equations are as follows;

Continuity equation;

$$\partial\rho/\partial t + \nabla\cdot(\rho u) = 0 \tag{15}$$

where ρ is the density and u are the velocity vector, u=(u,v), the operator ∇ is (∂/∂x, ∂/∂y)

Momentum equation;

$$\partial(\rho u)/\partial t + \nabla\cdot(\rho uu) = -\nabla p + \nabla\cdot(\mu_{eff}\nabla u) + F \tag{16}$$

where p is the pressure, μ_{eff} is the effective viscosity ($\mu_{eff} = \mu + \mu_t$) and F presents body forces.

Energy equation;

$$\partial(\rho E)/\partial t + \nabla\cdot(u(\rho E+p)) = \nabla\cdot(k_{eff}\nabla T) + S \tag{17}$$

where E is the total energy per unit mass, k is the effective thermal conductivity ($k_{eff} = k + k_t$), T is the temperature, S is a source term.

The VOF method is used to track the interface between the two phases. The volume fraction of the primary phase (liquid) is denoted by α, and the volume fraction of the secondary phase (gas) is (1−α). Therefore, the volume fraction equation is;

$$\partial\alpha/\partial t + u\cdot\nabla\alpha = 0 \tag{18}$$

The k-ε realizable turbulence model is used to simulate turbulent flow. It introduces two transport equations for turbulent kinetic energy and its dissipation rate.

Turbulent kinetic energy equation;

$$\partial(\rho k)/\partial t + \nabla\cdot(\rho k u) = \nabla\cdot((\mu_t/\sigma_k)\nabla k) + Pk - \rho\epsilon \tag{19}$$

Dissipation rate equation;

$$\partial(\rho\epsilon)/\partial t + \nabla\cdot(\rho\epsilon u) = \nabla\cdot((\mu_t/\sigma_\epsilon)\nabla\epsilon) + C_1 P_k \epsilon/k - C_2\rho\epsilon^2/k \tag{20}$$

where μ_t is the turbulent viscosity, P_k is the production of turbulence kinetic energy, C_1 and C_2 are model constants, σ_k and σ_ϵ are the turbulent Prandtl numbers for k and ϵ.

$C_1 = 1.44$ and $C_2 = 1.9$

2.4.2.1. Boundary conditions

Pressure inlet boundary conditions were applied at both the primary and secondary inlets, and a pressure outlet boundary condition was used for the ejector exit. The corresponding pressure values were defined using the experimental data for each condenser temperature. In the simulations, the condenser temperature varied between 25°C and 47°C. Accordingly, the primary inlet pressure ranged from 533 kPa to 980 kPa, the secondary inlet pressure from 411 kPa to 534 kPa, and the outlet pressure from 420 kPa to 563 kPa. All pressure values were specified as absolute pressures. Furthermore, adiabatic wall conditions were assumed, neglecting any heat transfer through the ejector walls. The flow directions at both the primary and secondary inlets were assumed to be normal to the boundary. Turbulence parameters were specified using a turbulent viscosity ratio of 10 and a turbulence intensity of 5%.

2.4.2.2. Solution procedure

A pressure-based solver was selected for the simulations, and the SIMPLE algorithm was used for pressure-velocity coupling due to its efficiency in convergence behavior. The iterative solution process was continued until the residuals for continuity, momentum, energy, and other governing equations were reduced below 1×10^{-6}. Once the first conditions were defined, a hybrid initialization method was applied, after which the simulations were run. The thermophysical properties of the refrigerant are given in Table 3.

Table 3. Thermo-physical properties of R134a [39]

	R134a
Composition	-
Mass percentage (%)	-
Critical pressure (kPa)	4059.3
Boiling point (K)	247.1
Vapour density ($kg\cdot m^{-3}$)	32.35
Critical temperature (K)	374.2
Vapour conductivity ($W\cdot m^{-1}\cdot K^{-1}$)	$81.13\cdot10^{-3}$
Cp liquid ($kJ\cdot kg^{-1}\cdot K^{-1}$)	1.425
Liquid density ($kg\cdot m^{-3}$)	1206.7
Cp vapour ($kJ\cdot kg^{-1}\cdot K^{-1}$)	1.032
Liquid conductivity ($W\cdot m^{-1}K^{-1}$)	$13.83\cdot10^{-3}$
Latent heat value ($kJ\cdot kg^{-1}$)	216.9
GWP	1300
ASHRAE Safety class	A1

2.4.3. Model validation

To ensure the accuracy of the numerical predictions, model validation is crucial. This section compares the results obtained from the CFD simulations with corresponding experimental data. Figure 8 shows pressure contours through the ejector for different condenser temperatures: 44.0-40.2-30.4-25.2°C respectively, from left to right. Pressure difference (motive-outlet) was selected for validation due to its critical influence on ejector performance. Figure 9 presents the pressure difference variations predicted by the simulations and measured experimentally across a range of condenser temperatures. The CFD results show good agreement with the experimental data, with a coefficient of determination (R^2) of 0.986 and a root mean square error (RMSE) of 12.46 kPa. The numerical calculations match the experiments closely at lower condenser temperatures, although a slight increase in deviation is seen as the condenser temperature rises. Nevertheless, the differences stay within an acceptable range. These differences may be attributed to several simplifying assumptions used in the CFD model, which are listed below:

- Adiabatic walls: Heat transfer through the ejector walls is neglected.
- Steady-state flow: The model assumes constant operating conditions over time.
- Suction chamber mixing: Perfect mixing of the flow is assumed within the suction chamber.

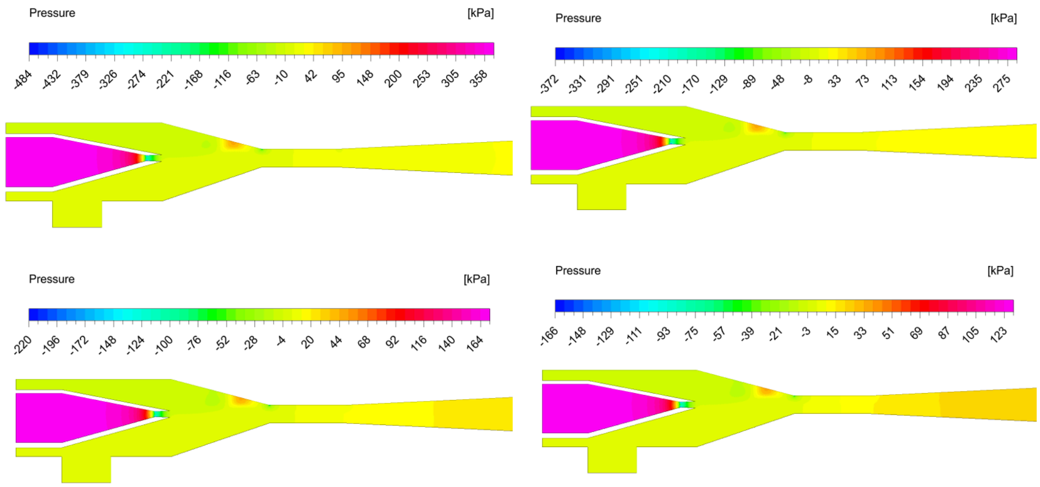

Figure 8. Pressure contours of ejectors for different condenser temperature

3. Results and discussion

After completing both the experimental tests and CFD simulations, all data were collected and analyzed with respect to three main aims. First, the variation of isentropic efficiencies for different ejector components as a function of condenser temperature was examined. Second, empirical correlations were developed to predict these efficiencies over the range of condenser temperatures. Third, the influence of ejector part efficiencies on system performance was assessed.

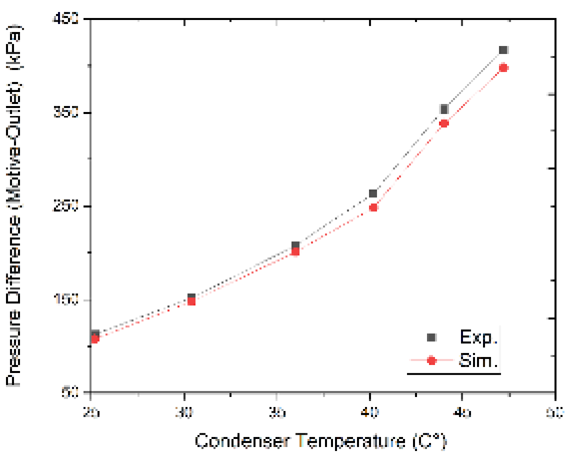

Figure 9. Validation of simulation results by experimental results

3.1. The changes of isentropic efficiencies of various parts of the ejector depending on the condenser temperature

Figure 10 shows the variation of isentropic efficiencies of the ejector components as a function of condenser temperature. As seen in Figure 10, η_{sc}, η_{mc}, η_d all increase with rising condenser temperature. However, η_{mn} shows a slight decrease, while η_{sfo} drops sharply. The reduction in η_{sfo} can mainly be due to the increase in refrigerant density. Since the ER is kept constant, a stronger vacuum is generated at the secondary inlet of the ejector, which in turn leads to a reduction in η_{sfo}. On the other hand, increasing condenser temperature reduces the latent heat of the refrigerant. As a result, the enthalpy difference between the saturated liquid (x = 0) and saturated vapor (x = 1) states decreases, while entropy stays unchanged. Because of this reduced enthalpy range, the diffuser outlet enthalpy moves closer to the isentropic reference line. This explains the observed improvement in η_d, as shown in Figure 10. The specific enthalpy of the diffuser outlet was calculated using Equations 21.

$$h_7 = \frac{h_{7,is} - h_6}{\eta_d} + h_6 \tag{21}$$

where η_d is diffuser isentropic efficiency, calculated by Eq.5, $h(_{7,is})$ isentropic value, obtained from experimental results, h_6 is mixing chamber enthalpy, obtained from simulation results.

This section explains the reason for the use of the simulated mixing chamber enthalpy value ($h_{6,sim}$) in Eq. 21 instead of the experimentally measured value ($h_{6,is}$). The specific enthalpy at the ejector outlet (h_7) was calculated by both experimental data ($h_{6,is}$) and CFD simulations ($h_{6,sim}$) as seen in Eq.21. The actual specific enthalpy at the ejector outlet ($h_{7actual}$) was decided from the temperature difference between the inlet and outlet of the evaporator #2 water loop. As shown in Figure 11, a comparison of these values shows that $h_{7,sim}$ is in closer agreement with $h_{7actual}$ than $h_{7,is}$. This better agreement between the simulated and measured enthalpies supports the use of $h_{6,sim}$ for deciding the specific enthalpy at the diffuser outlet using Equation (21). The reduction in η_{sfo} is mainly attributed to the increase in condenser pressure, which also leads to a rise in evaporation pressure in evaporator #1. This pressure increase results in higher refrigerant density, which weakens the entrainment capability of the ejector and so reduces the isentropic efficiency in this region.

3.2. Derivation of empirical equations for isentropic efficiency calculations

Eleven sets of experiments were carried out at condenser temperatures ranging from 23°C to 50°C. The resulting correlations are presented in Table 4 and can be used to estimate the isentropic efficiencies of different ejector components as a function of condenser temperature. Moreover, these correlations also enable the estimation of key thermodynamic parameters, including diffuser outlet pressure, vapor quality, and mixing chamber pressure. All other operating conditions were kept constant throughout the experiments, with condenser temperature being the only varying parameter in the developed equations.

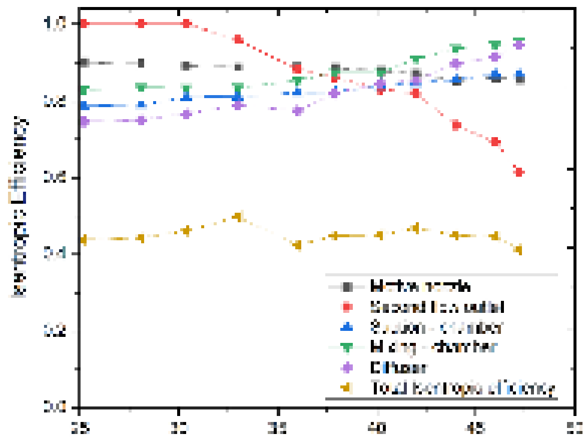

Figure 10. Changes of isentropic efficiencies of various parts of the ejector depending on the condenser temperature

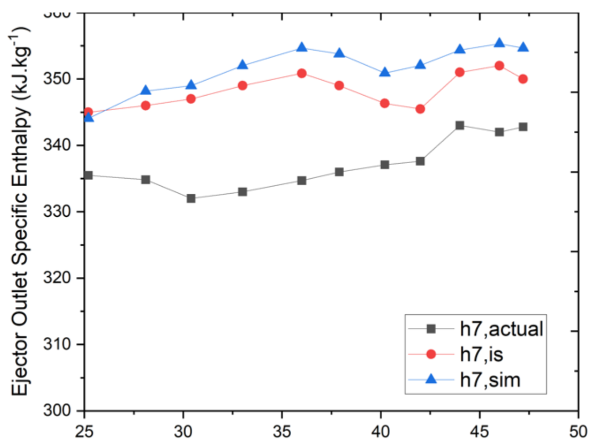

Figure 11. Comparison of ejector outlet specific enthalpy: actual, simulated, and experimental

Table 4. Empirical equations derived from several parts of the ejector

Ejector efficiencies	Empirical correlations	R^2	Equation numbers
η_{mn}	$y = -0.0022x + 0.9599$	0.88	22
η_{sfo}	$y = -0.0007x^2 + 0.0343x + 0.5895$	0.98	23
η_{sc}	$y = 0.0038x + 0.6865$	0.97	24
η_{mc}	$y = 0.0003x^2 - 0.0163x + 1.0447$	0.97	25
η_d	$y = 0.009x + 0.4924$	0.91	26
P_{mc}	$y = 29.08e^{0.0584x}$	0.99	27
X_{mc}	$y = -0.0001x + 0.5391$	0.98	28
P_d	$y = -0.2401x^2 + 23.89x - 37.045$	0.98	29

This section employed simulation results to develop empirical equations for both mixing chamber pressure (Eq. 27) and mixing chamber quality (Eq. 28) across a range of condenser temperatures. These equations are valuable tools for ejector analysis, as they allow for the determination of one of the critical parameters, the specific enthalpy at the diffuser outlet. It can be decided by the following steps given below. The following steps outline the determination process.

First, REFPROP utilizes the results from Eq. 27 and 28 to obtain the mixing chamber's enthalpy and entropy values.

$$h_{mixing\ chamber,}\ s_{mixing\ chamber} = f(P_{sim,mixing\ chamber}, x_{sim,mixing\ chamber}) \quad (30)$$

Building upon the first step, Eq. 31 allows for the calculation of the diffuser outlet's isenthalpic enthalpy value. This equation requires the mixing chamber entropy value (obtained from Eq. 30) and the diffuser outlet pressure value (obtained from Eq. 29) as inputs.

$$h_{dif,out,is} = f(P_{dif,out}, s_{mixing\ chamber}) \quad (31)$$

The final step is the calculation of the diffuser outlet specific enthalpy using Eq. 32. This equation combines the diffuser isentropic efficiency, obtained from Eq. 26, with the diffuser outlet isenthalpic enthalpy value, calculated from Eq. 31, as input.

$$h_{dif,out} = (h_{dif,out,is} - h_{mixing\ chamber})/\eta_{dif} + h_{mixing\ chamber} \quad (32)$$

3.3. Investigating the effect of isentropic efficiencies on ejector system performance parameters

This section examines the effect of variations in the isentropic efficiencies of different ejector components on system performance. Table 5 summarizes the changes in evaporator #2 cooling capacity and degree of superheat recorded at eleven different condenser temperatures. Additionally, the mixing chamber and diffuser isentropic efficiencies were calculated for these corresponding condenser temperatures. Figure 12 is the changes in evaporator#2 cooling capacity and degree of superheat in relation to the mixing chamber isentropic efficiency and the diffuser isentropic efficiency, respectively.

Figure 12(a) outlines that evaporator#2 cooling capacity per unit refrigerant mass decreases as the η_{mc} increases. This behavior can be explained by the interaction between mixing chamber efficiency and refrigerant quality. As η_{mc} increases, the quality of the refrigerant at the mixing chamber outlet decreases (X_{mc}). Since η_d was applied to the mixing chamber enthalpy value, it directly affected the quality degree at the ejector outlet. Consequently, the refrigerant leaves the ejector at a lower quality value, evaporator#2 capacity per unit mass increases.

Figure 12(b) depicts the opposite trend: the degree of superheat of evaporator#2 decreases with increasing diffuser efficiency (η_d). This can be understood by considering the behavior of the diffuser as it approaches isentropic conditions ($\eta_d \rightarrow 1$). As a result, to keep a constant cooling capacity value, the degree of superheat of evaporator#2 needs to decrease.

Table 5. Changes of performance parameters at varying condenser temperature

Condenser Temperature (C°)	$Q_{evap\#2,net}$	Superheating degree$_{evap\#2}$
25.2	68.07	8.11
28.2	65.31	8.74
30.4	64.25	7.55
33.0	62.00	7.20
36.0	59.91	6.85
37.9	59.02	4.56
40.2	59.08	1.03
42	58.21	1.33
44	55.39	0.91
46	55.06	1.49
47.2	55.02	0.19

4. Conclusion

This study examined the influence of isentropic efficiencies of individual ejector components on the performance of evaporator #2. To this end, the efficiencies of different ejector sections were evaluated over a range of condenser temperatures. This allowed the relationship between condenser temperature and overall ejector behavior to be clarified. In addition, the resulting effects on evaporator #2 performance indicators, such as cooling capacity per unit refrigerant mass and degree of superheat, were evaluated. To support the analysis, empirical correlations were developed to predict key ejector operating parameters as a function of condenser temperature. The reliability of these correlations was then verified using both experimental measurements and CFD results.

The results show that the isentropic efficiencies of the suction chamber (η_{sc}), mixing chamber (η_{mc}), and diffuser (η_d) increase with rising condenser temperature. However, the efficiencies of the motive nozzle (η_{mn}) and secondary flow outlet (η_{sfo}) decrease. Except for η_{sfo}, all part efficiencies are in the range of 0.80 to 0.95, while η_{sfo} varies between 0.60 and 1.00. In addition, the degree of superheat decreases from 8.74 K to 0.19 K as condenser temperature increases, while the cooling capacity of evaporator #2 reduces from 68.02 to 55.07 kJ.kg^{-1}. These trends indicate an inverse relationship between condenser temperature and both superheat level and evaporator cooling performance.

A vital contribution of this work is the development of empirical correlations that may be used to estimate ejector part efficiencies for different operating conditions and geometries. However, a limitation of this study is that both experimental and numerical analyses were carried out using a single refrigerant. Future work should continue this investigation to include alternative refrigerants with lower GWP values.

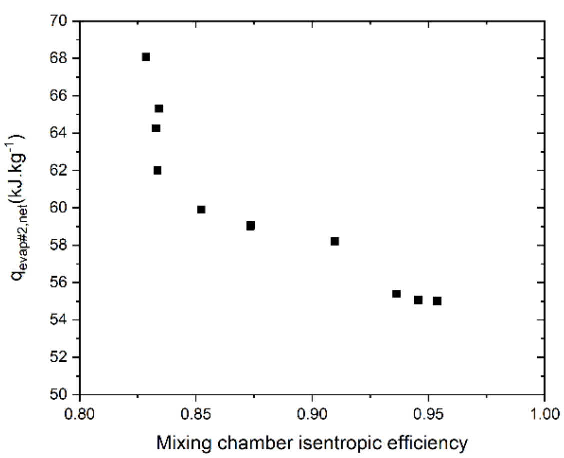

(a)

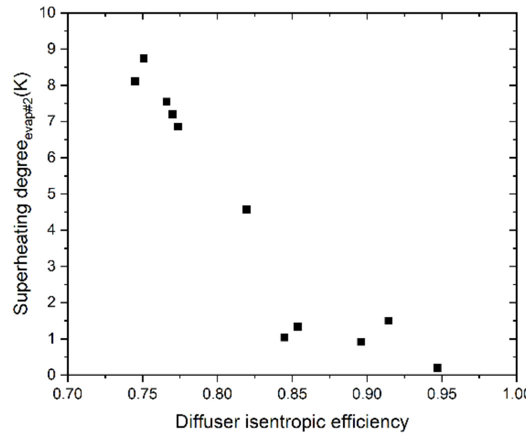

(b)

Figure 12. Changes in **a)** mixing chamber isentropic efficiency & cooling capacity per unit mass in Evap#2 **b)** Diffuser isentropic efficiency & Evaporator#2 degree of superheat

Acknowledgement

We are grateful to Yalova University due to financial support (Project no: 2022/AP/0010 and 2023/YL/0002).

Author contributions statement

Mahmut Cüneyt Kahraman: Data Curation, Methodology, CFD Modelling, Formal Analysis, Writing-Original Draft Preparation, Supervision. Ümit İşkan: Data Curation, Conceptualization, Validation, Experimental Tests, Writing – Review & Editing. Mehmet Direk: Conceptualization, Visualization, Project Administration, Writing-Review & Editing, Supervision

Declaration of interest

The authors declare that they have no known competing financial interests or personal relationships that could have appeared to influence the work reported in this paper.

Data availability statement

Data will be made available on request.

Declaration of generative AI and AI-assisted technologies in the writing process

The authors acknowledge the use of AI tools strictly for the purposes of English language editing, proofreading, and improving the overall readability of this manuscript. The AI tools were not used for data generation, mathematical calculations or modeling. The author carefully reviewed all AI-assisted edits and takes full responsibility for the final integrity and content of the article.

References

[1] J. Chen, H. Havtun, ve B. Palm, "Screening of working fluids for the ejector refrigeration system", International Journal of Refrigeration, c. 47, sayı 0, ss. 1–14, 2014, doi: 10.1016/j.ijrefrig.2014.07.016.

[2] P. Haghparast, M. V. Sorin, ve H. Nesreddine, "The impact of internal ejector working characteristics and geometry on the performance of a refrigeration cycle", Energy, c. 162, ss. 728–743, 2018, doi: 10.1016/j.energy.2018.08.017.

[3] S. Elbel ve P. Hrnjak, "Experimental validation of a prototype ejector designed to reduce throttling losses encountered in transcritical R744 system operation", International Journal of Refrigeration, c. 31, sayı 3, ss. 411–422, 2008, doi: 10.1016/j.ijrefrig.2007.07.013.

[4] V. Jain, S. Khurana, A. Parinam, G. Sachdeva, A. Goel, ve K. Mudgil, "Experimental analysis of an ejector assisted dual-evaporator vapor compression system", Energy Conversion and Management, c. 300, sayı November 2023, s. 117966, 2024, doi: 10.1016/j.enconman.2023.117966.

[5] B. H. B. Alphonse, R. B. Rayappa, H. Koten, R. Balasubramanian, ve D. U. Sarwe, "Comparative Design and Cfd Analysis of 3-D Printed Acrylonitrile Butadiene Styrene Nozzle Aerator for Discharge Reduction", Thermal Science, c. 26, sayı 2, ss. 857–869, 2022, doi: 10.2298/TSCI201114155A.

[6] H. Li, F. Cao, X. Bu, L. Wang, ve X. Wang, "Performance characteristics of R1234yf ejector-expansion refrigeration cycle", Applied Energy, c. 121, ss. 96–103, 2014, doi: 10.1016/j.apenergy.2014.01.079.

[7] F. Liu ve E. A. Groll, "Study of ejector efficiencies in refrigeration cycles", Applied Thermal Engineering, c. 52, sayı 2, ss. 360–370, 2013, doi: 10.1016/j.applthermaleng.2012.12.001.

[8] K. Banasiak, A. Hafner, ve T. Andresen, "Experimental and numerical investigation of the influence of the two-phase ejector geometry on the performance of the R744 heat pump", International Journal of Refrigeration, c. 35, sayı 6, ss. 1617–1625, 2012, doi: 10.1016/j.ijrefrig.2012.04.012.

[9] Ş. Ünal, E. Cihan, M. T. Erdinç, ve M. Bilgili, "Influence of mixing section inlet and diffuser outlet velocities on the performance of ejector-expansion refrigeration system using zeotropic mixture", Thermal Science and Engineering Progress, c. 33, sayı May, 2022, doi: 10.1016/j.tsep.2022.101338.

[10] N. Galanis ve M. Sorin, "Ejector design and performance prediction", International Journal of Thermal Sciences, c. 104, ss. 315–329, 2016, doi: 10.1016/j.ijthermalsci.2015.12.022.

[11] J. Liu, L. Wang, L. Jia, ve X. Wang, "The influence of the area ratio on ejector efficiencies in the MED-TVC desalination system", Desalination, c. 413, ss. 168–175, 2017, doi: 10.1016/j.desal.2017.03.017.

[12] X. Wang ve J. Yu, "An investigation on the component efficiencies of a small two-phase ejector Une étude de l ' efficacité des composants d ' un petit éjecteur diphasique", International Journal of Refrigeration, c. 71, ss. 26–38, 2016, doi: 10.1016/j.ijrefrig.2016.08.006.

[13] H. Zhang, L. Wang, L. Jia, ve X. Wang, "Assessment and prediction of component efficiencies in supersonic ejector with friction losses", Applied Thermal Engineering, c. 129, ss. 618–627, 2018, doi: 10.1016/j.applthermaleng.2017.10.054.

[14] B. Kitrattana, S. Aphornratana, ve T. Thongtip, "One dimensional steam ejector model based on real fluid property", Thermal Science and Engineering Progress, c. 25, sayı September 2020, s. 101016, 2021, doi: 10.1016/j.tsep.2021.101016.

[15] A. Bauzvand, E. Tavousi, A. Noghrehabadi, ve M. Behbahani-Nejad, "Study of a novel inlet geometry for ejectors", International Journal of Refrigeration, c. 139, sayı February, ss. 113–127, 2022, doi: 10.1016/j.ijrefrig.2022.04.011.

[16] H. Zhang, L. Wang, L. Jia, H. Zhao, ve C. Wang, "Influence investigation of friction on supersonic ejector performance Étude de l ' influence de la friction sur la performance d ' un éjecteur supersonique", International Journal of Refrigeration, c. 85, ss. 229–239, 2018, doi: 10.1016/j.ijrefrig.2017.09.028.

[17] E. Bumrungthaichaichan, N. Ruangtrakoon, ve T. Thongtip, "Performance investigation for CRMC and CPM ejectors applied in refrigeration under equivalent ejector geometry by CFD simulation", Energy Reports, c. 8, ss. 12598–12617, 2022, doi: 10.1016/j.egyr.2022.09.042.

[18] J. Feng, J. Han, T. Hou, ve X. Peng, "Environmental Effects Performance analysis and parametric studies on the primary nozzle of ejectors in proton exchange membrane fuel cell systems", Energy Sources, Part A: Recovery, Utilization, and Environmental Effects, c. 00, sayı 00, ss. 1–20, 2020, doi: 10.1080/15567036.2020.1804489.

[19] C. P. Rand, S. Croquer, ve M. Poirier, "Optimal nozzle exit position for a single-phase ejector (Experimental , numerical and thermodynamic modelling)", c. 144, sayı August, ss. 108–117, 2022, doi: 10.1016/j.ijrefrig.2022.08.014.

[20] M. Atmaca ve C. Ezgi, "Environmental Effects Three-dimensional CFD modeling of a steam ejector", Energy Sources, Part A: Recovery, Utilization, and Environmental Effects, c. 44, sayı 1, ss. 2236–2247, 2022, doi: 10.1080/15567036.2019.1649326.

[21] C. Vereda, R. Ventas, A. Lecuona, ve M. Venegas, "Study of an ejector-absorption refrigeration cycle with an adaptable ejector nozzle for different working conditions", Applied Energy, c. 97, ss. 305–312, 2012, doi: 10.1016/j.apenergy.2011.12.070.

[22] K. Ameur, Z. Aidoun, ve M. Ouzzane, "Experimental performances of a two-phase R134a ejector", Experimental Thermal and Fluid Science, c. 97, sayı April, ss. 12–20, 2018, doi: 10.1016/j.expthermflusci.2018.03.034.

[23] K. Ameur ve Z. Aidoun, "Two-phase ejector enhanced carbon dioxide transcritical heat pump for cold climate", Energy Conversion and Management, c. 243, s. 114421, 2021, doi: 10.1016/j.enconman.2021.114421.

[24] L. Zheng, Y. Hu, C. Mi, ve J. Deng, "Advanced exergy analysis of a CO2 two-phase ejector", Applied Thermal Engineering, c. 209, sayı February, s. 118247, 2022, doi: 10.1016/j.applthermaleng.2022.118247.

[25] M. Wang, Y. Cheng, ve J. Yu, "Analysis of a dual-temperature air source heat pump cycle with an ejector", Applied Thermal Engineering, c. 193, sayı April, s. 116994, 2021, doi: 10.1016/j.applthermaleng.2021.116994.

[26] A. Surendran ve S. Seshadri, "An ejector based Transcritical Regenerative Series Two-Stage Organic Rankine Cycle for dual/multi-source heat recovery applications", Thermal Science and Engineering Progress, c. 27, sayı August 2021, s. 101158, 2022, doi: 10.1016/j.tsep.2021.101158.

[27] N. Bilir ve H. K. Ersoy, "Performance improvement of the vapour compression refrigeration cycle by a two-phase constant area ejector", International Journal of Energy Research, c. 33, sayı 5, ss. 469–480, 2009, doi: 10.1002/er.1488.

[28] Ş. Ünal ve T. Yilmaz, "Thermodynamic analysis of the two-phase ejector air-conditioning system for buses", Applied Thermal Engineering, c. 79, ss. 108–116, 2015, doi: 10.1016/j.applthermaleng.2015.01.023.

[29] Ü. İşkan ve M. Direk, "Experimental performance evaluation of the dual-evaporator ejector refrigeration system using environmentally friendly refrigerants of R1234ze(E), ND, R515a, R456a, and R516a as a replacement for R134a", Journal of Cleaner Production, c. 352, sayı January, 2022, doi: 10.1016/j.jclepro.2022.131612.

[30] B. Üğüdür ve M. DiRek, "Comparative evaluation of experimental ejector refrigeration system for different operating configurations", Journal of Thermal Engineering, c. 10, sayı 2, ss. 321–329, 2023, doi: 10.18186/THERMAL.1448602.

[31] N. Bilir Sag, H. K. Ersoy, A. Hepbasli, ve H. S. Halkaci, "Energetic and exergetic comparison of basic and ejector expander refrigeration systems operating under the same external conditions and cooling capacities", Energy Conversion and Management, c. 90, ss. 184–194, 2015, doi: 10.1016/j.enconman.2014.11.023.

[32] J. Yan, C. Lin, W. Cai, H. Chen, ve H. Wang, "Experimental study on key geometric parameters of an R134A ejector cooling system", International Journal of Refrigeration, c. 67, ss. 102–108, 2016, doi: 10.1016/j.ijrefrig.2016.04.001.

[33] Ü. Işkan ve M. Direk, "Experimental investigation on the effect of expansion valves in a dual evaporator ejector refrigeration system using R134a and R456a", Energy Sources, Part A: Recovery, Utilization and Environmental Effects, c. 47, sayı 1, ss. 2364–2378, 2021, doi: 10.1080/15567036.2021.1982076.

[34] L. Geng, H. Liu, ve X. Wei, "CFD analysis of the flashing flow characteristics of subcritical refrigerant R134a through converging-diverging nozzles", International Journal of Thermal Sciences, c. 137, sayı December 2018, ss. 438–445, 2019, doi: 10.1016/j.ijthermalsci.2018.12.011.

[35] N. Ruangtrakoon, T. Thongtip, S. Aphornratana, ve T. Sriveerakul, "CFD simulation on the effect of primary nozzle geometries for a steam ejector in refrigeration cycle", International Journal of Thermal Sciences, c. 63, ss. 133–145, 2013, doi: 10.1016/j.ijthermalsci.2012.07.009.

[36] NASA,Examining Spatial (Grid) Convergence, https://www.grc.nasa.gov/www/wind/valid/tutorial/spatconv.html, 2021

[37] ANSYS 2019 R2. 2019. Fluent Theory Guide. 2019 R2. https://ansyshelp.ansys.com/account/secured returnurl=/Views/Secured/corp/v194/flu_th/flu_th_sec_melt_theory.html.

[38] A. Hemidi, F. Henry, S. Leclaire, J. M. Seynhaeve, ve Y. Bartosiewicz, "CFD analysis of a supersonic air ejector. Part I: Experimental validation of single-phase and two-phase operation", Applied Thermal Engineering, c. 29, sayı 8–9, ss. 1523–1531, 2009, doi: 10.1016/j.applthermaleng.2008.07.003.

[39] LEMMON E W, HUBER M L, MCLINDEN M O. NIST Standard Reference Database 23, NIST Reference Fluid Thermodynamic and Transport Properties. REFPROP version 10.0,

Appendices

Nomenclature

$\dot{Q}$	Capacity
C	Model Constant
CFD	Computational Fluid Dynamics
COP	Coefficient of Performance
D	Dimension
DEES	Dual evaporator ejector system
ER	Entrainment Ratio
FS	Factor of safety
GCI	Grid Convergence Index
GWP	Global Warming Potential
K	Kelvin
P	Pressure
P	Point
PID	Proportional Integral Derivative
RANS	Reynolds-Averaged Navier Stokes
R^2	Coefficient of Determination
SST	Shear Stress Transport
T	Temperature
TXV	Thermal Expansion Valve
VOF	Volume of fluid
W	Watt
η	Isentropic efficiency
σ	Prandtl number
μt	Turbulent viscosity
$\dot{m}$	Mass flow rate
Comp	Compressor
Cond	Condenser
d	diffuser
Eq	Equation
Evap	Evaporator
Exp	Experiment
f	Function
h	Enthalpy
is	isentropic
kg	kilogram
kJ	kilojoule
m	meter
mc	mixing chamber

mn	motive nozzle
RMSE	Root Mean Square Error
Pa	Pascal
r	Refinement ratio
sc	suction chamber
sfo	second flow outlet
sim	Simulation
x	Quality